Photoexcitation and ionization in ozone: Stieltjes–Tchebycheff studies in the separated-channel static-exchange approximation

N. Padial and G. Csanak

Instituto de Física, Universidade Estadual de Campinas, Campinas, Brazil

B. V. McKoy

Arthur Amos Noyes Laboratory of Chemical Physics, California Institute of Technology, Pasadena, California 91125

P. W. Langhoff

Department of Chemistry,[a] Indiana University, Bloomington, Indiana 47405,
Computational Chemistry Group, NASA Ames Research Center, Moffett Field, California 94035,
and Department of Aeronautics and Astronautics, Stanford University, Stanford, California 94305

Theoretical studies are reported of total and partial-channel photoexcitation/ionization cross sections in ozone employing Stieltjes–Tchebycheff (S–T) techniques and the separated-channel static-exchange approximation. As in previously reported investigations of excitation and ionization spectra in diatomic and polyatomic molecules employing this approach, vertical electronic dipole transition spectra for the twelve occupied canonical Hartree–Fock symmetry orbitals in ozone are constructed using large Gaussian basis sets, appropriate computational methods, and noncentral static-exchange potentials of correct molecular symmetry. Experimental rather than Koopmans ionization potentials are employed when available in construction of transition energies to avoid the incorrect ionic-state orderings predicted by Hartree–Fock theory, and to insure that the calculated series have the appropriate limits. The spectral characteristics of the resulting improved-virtual-orbital discrete excitation series and corresponding static-exchange photoionization continua are interpreted in terms of contributions from valencelike $7a_1(\sigma^*)$, $2b_1(\pi_x^*)$, and $5b_2(\sigma^*)$ virtual orbitals, and appropriate diffuse Rydberg functions. The $2b_1(\pi_x^*)$ valence orbital apparently contributes primarily to discrete or autoionizing spectra, whereas the $7a_1(\sigma^*)$ and $5b_2(\sigma^*)$ orbitals generally appear in the various photoionization continua. Moreover, there is also evidence of strong $2p \rightarrow kd$ atomiclike contributions to ka_2 final-state channels in the photoionization continua. The calculated outer-valence-shell $6a_1$, $4b_2$, and $1a_2$ excitation series are compared with electron impact–excitation spectra in the 9 to 13 eV interval, and the corresponding partial-channel photoionization cross sections are contrasted and compared with the results of previously reported studies of photoionization in molecular oxygen. The intermediate- and inner-valence-shell excitation series and corresponding photoionization cross sections are in general accord with quantum-defect estimates and with the measured electron-impact spectra, which are generally unstructured above ~ 22 eV. Of particular interest in the intermediate-valence-shell spectra is the appearance of a strong $\sigma \rightarrow \sigma^*$ feature just above threshold in the $3b_2 \rightarrow kb_2$ photoionization cross section, in qualitative agreement with previously reported studies of the closely related $3\sigma_g \rightarrow k\sigma_u$ cross section in molecular oxygen. Finally, qualitative comparisons are made of the calculated K-edge excitation and ionization spectra in ozone with recently reported photoabsorption studies in molecular oxygen.

I. INTRODUCTION

Molecular ozone is one of the more important trace constituents of the earth's atmosphere.[1] In spite of this, many aspects of its photoabsorption spectrum and photochemistry are incompletely understood at present.[2,3] Specifically, although photoabsorption,[4-10] photoionization,[11-14] and electron-impact cross sections[15,16] have been measured, certain regions of the spectrum analyzed,[17] and theoretical investigations of the ground and low-lying excited states reported,[18-32] very little is known about the higher-lying excited states and the various partial-channel photoionization continua. Theoretical studies of the far UV dipole excitation/ionization spectrum in ozone at a computationally reliable level of approximation would clearly be desirable.

In the present article, theoretical investigations of

vertical electronic photoexcitation and ionization in O_3 are reported employing static-exchange calculations and the Stieltjes–Tchebycheff (S–T) technique.[33-35] As in previously reported studies of diatomic (N_2, CO, O_2, F_2)[36-42] and polyatomic (H_2O, H_2CO)[43-45] molecules employing this approach, large Gaussian basis sets, Hartree–Fock canonical orbitals, and appropriate computational methods[46,47] are used in constructing many-electron wave functions and noncentral static-exchange potentials of correct symmetry for the excitation and ionization of the occupied orbitals in O_3. Although the Hartree–Fock approximation provides an incorrect ordering of certain of the low-lying neutral and ionic states in O_3 and does not provides a completely adequate description of the biradical character of its ground state,[26-28] the canonical orbitals should give generally appropriate hole states for calculations of higher-lying discrete spectra and corresponding photoionization continua. Variational solutions of the one-electron excita-

tion/ionization equations provide improved-virtual-orbital (IVO) discrete states[48-51] and pseudospectral approximations to the static-exchange continua, from which the corresponding photoionization cross sections are obtained using the S–T technique.[35] Experimental rather than Koopmans ionization potentials are employed for the outer-valence orbitals[11-14] to avoid the incorrect ionic-state orderings indicated above, to allow somewhat for the effects of core relaxation,[52] and to insure that the calculated series and continua have appropriate limits and thresholds. Although the vertical-electronic separated-channel static-exchange approximation can be refined and improved upon, experience indicates the approach is generally satisfactory for the excitation and ionization of outer-valence and K-shell orbitals.[36-45] When the effects of valence configuration mixing are important, it is possible to retain the simplicity of the static-exchange approach by introducing an appropriate projection-operator technique.[42] Moreover, for inner-valence-shell ionization, in which cases the effects of correlation are more significant and the orbital model can fail completely,[52] the static-exchange results can be employed in conjunction with appropriate ionic-state shakeup amplitudes in obtaining first approximations to the cross sections. Finally, the vertical-excitation results can be combined with bound and dissociative Franck–Condon factors to obtain the yields of molecular ions and ionic-fragment products. Consequently, it is seen that S–T static-exchange calculations provide the initial information necessary for construction of reliable cross sections over the entire allowable ionization spectrum in O_3.

The calculated discrete excitations are found to be comprised of nsa_1, npa_1, npb_1, npb_2, and nda_2 Rydberg series and generally stronger transitions into $2b_1(\pi_x^*)$ and $5b_2(\sigma^*)$ valencelike virtual orbitals. There is general agreement between the predicted $6a_1$, $4b_2$, $1a_2$ $\rightarrow na_1$, nb_1, and nb_2 outer-valence Rydberg series and quantum-defect estimates,[53,54] and the positions of strong $6a_1 \rightarrow 5b_2(\sigma^*)$ and $1a_2 \rightarrow 2b_1(\pi_x^*)$ intravalence transitions are in accord with prominent features in the electron-impact data.[15] However, as indicated above, the positions of intravalence states can be sensitive to the effects of configuration interaction, and in certain cases the static-exchange approach requires modification.[42] These aspects of the static-exchange approximation in the case of O_3, and techniques for avoiding the difficulties that can arise are discussed at appropriate points in the text. Although the higher Rydberg excitation series associated with inner-valence orbitals have not been experimentally assigned, the calculated positions and intensities are in general accord with the measured spectra and with estimates based on quantum-defect analysis.[53,54] Of course, autoionizing line-shape calculations are generally required in these cases to obtain intensity profiles appropriate for detailed comparison with experiment.

Certain of the calculated partial-channel photoionization cross sections exhibit resonancelike structures that can be attributed to contributions from valencelike $7a_1(\sigma^*)$ and $5b_2(\sigma^*)$ virtual orbitals in the appropriate continua. In addition, there is evidence of strong atomiclike $2p$

$\rightarrow kd$ contributions to the ka_2 final-state photoionization profiles. Although corresponding experimental partial-channel cross sections are not available for comparison with the calculations, the theoretical results are in qualitative accord with previously reported studies of photoionization in other polyatomic molecules (H_2O, H_2CO) having C_{2v} symmetry[43,45] and are similar in certain respects to the previously studied partial-channel cross sections in molecular oxygen.[40,41] Moreover, in spite of the various structures in the partial-channel components, the calculated total photoionization cross section is generally structureless in the 22–30 eV interval, in qualitative accord with the photoabsorption and electron-impact measurements.[4-10,15,16]

Although further computational refinements, including the effects of configuration-interaction on intravalence transitions, incorporation of the biradical nature of the ground state in the calculations, determinations of shakeup amplitudes, explicit treatment of autoionizing intensities, and incorporation of aspects of the vibrational degrees of freedom will presumably alter certain of the quantitative aspects of the present study, the qualitative description provided here of the origins of the prominent features in the discrete and continuous spectra in ozone are likely to remain unchanged.

A brief description of the S–T separated-channel method is given in Sec. II, and the required IVO/static-exchange calculations in ozone are outlined in Sec. III. The resulting partial-channel and total photoexcitation/ionization cross sections are reported and discussed in Sec. IV, and concluding remarks are made in Sec. V.

II. THEORETICAL APPROACH

The Stieltjes–Tchebycheff procedure and the separated-channel static-exchange approximation are described in considerable detail in previous publications.[35-45] Consequently, only a brief description of the general scheme is presented here.

A ground-state Hartree–Fock function is constructed near the appropriate equilibrium molecular geometry employing Gaussian basis orbitals and appropriate computational methods.[46,47] Many-electron wave functions and noncentral static-exchange potentials are constructed from the self-consistent-field (SCF) canonical orbitals for each orbital excitation considered, and corresponding one-electron Schrödinger equations are formed for the calculation of excitation spectra. These equations are solved variationally employing basis sets significantly larger than those employed in constructing the ground-state Hartree–Fock function. Consequently, rather long integral files must generally be constructed in such calculations, involving storage and manipulation of many millions of words. This potential difficulty is avoided in the present development by constructing integral files for only those two-electron integrals in which two orbitals are taken from the occupied space and two from the virtual or unoccupied space, since these are the only ones required in the static-exchange calculations.[36,37]

The one-electron eigenvalues obtained from the static-exchange calculations that are below the occupied-orbital ionization potential, and the corresponding one-electron

orbitals, provide approximations to the appropriate discrete or autoionizing valence and Rydberg states. Those eigenvalues above the ionization potential, and their corresponding orbitals, provide pseudospectra for the Stieltjes–Tchebycheff moment analysis, from which the appropriate photoionization cross sections are obtained. Transition energies and oscillator strengths are formed employing experimental rather than Koopmans ionization potentials to avoid inadequacies in the Hartree–Fock predictions of the energy orderings of the ionic states. This procedure insures that the correct series limits and thresholds are incorporated and allows in some small measure for the effects of core relaxation and correlation energy differences in initial and final states. It is important to recognize, however, as indicated above, that static-exchange calculations can lead to incorrect positionings of intravalence states in dipole excitation spectra.[42] Valence basis configuration-interaction calculations, which do not involve the rather large basis sets required for a successful S–T analysis, can generally clarify the appropriate positioning of a particular state, and the IVO calculations can be interpreted accordingly.

The S–T approach employs a pseudospectrum of discrete transition frequencies and oscillator strengths, calculated in the present study as indicated in the preceding, in a smoothing procedure in which a continuous approximation to the underlying photoionization cross section is obtained. Conventional spectral power moments, which are convergent in the L^2 pseudospectrum of energies and strengths, are generally regarded as intermediaries in the smoothing procedure, providing a basis for establishing the convergence of the overall procedure. In actual calculations, however, the power moments are not used; rather, a highly stable computational algorithm is employed in constructing so-called recurrence coefficients and moment-theory spectra of (principal) frequency points and weights directly from the quantum-mechanically determined pseudospectrum.[33,34] These points and weights are the generalized Gaussian quadratures corresponding to the photoabsorption/ionization cross section. The moment-theory spectra exhibit useful properties which the original pseudospectrum does not exhibit and, in particular, provide bounds on the cumulative oscillator-strength distribution.[35] The bounds can be differentiated in a variety of ways to provide a final expression for the photoionization cross section. Stieltjes derivatives of various orders are generally employed to obtain a first approximation to the continuous cross section and to establish the range of convergence of the variationally calculated recurrence coefficients. Tchebycheff derivatives and appropriate recurrence-coefficient extension procedures are then used to construct a continuous approximation to the cross section. In addition, specific analytic forms fit to the cumulative Stieltjes histograms provide expressions convenient for differentiation. When very small numbers of recurrence coefficients or spectral moments are available, reference density techniques— in which additional available information is incorporated in the development—can also be employed.[55,56] Previous investigations indicate the general moment-theory ap-

proach is highly satisfactory, provided that the quantummechanical pseudostate calculation gives an adequate description of the underlying continuous spectrum.[33–45]

III. STATIC-EXCHANGE CALCULATIONS IN OZONE

The ground-state Hartree–Fock (HF) configuration in ozone is written

$$(1a_1^2 2a_1^2 1b_2^2 3a_1^2 2b_2^2 4a_1^2 5a_1^2 3b_2^2 1b_1^2 1a_2^2 4b_2^2 6a_1^2)^1A_1 , \tag{1}$$

where the molecular orbitals are ordered according to the observed photoelectron spectra when available.[11–14] Canonical Hartree–Fock orbitals are constructed in the present development at the experimental equilibrium geometry ($< = 116.8°$, $O–O = 2.413 a_0$)[57] in a (10s, 5p)/ [3s, 2p] Gaussian basis, giving a total SCF energy of -224.0898 a.u., compared to an experimental value of -225.562 a.u.[53] The energies and spatial characteristics of the occupied [Eq. (1)] and virtual ($2b_1$, $7a_1$, $5b_2$) valence orbitals have been given previously[18–25] and are only briefly described at appropriate points in the following. Of course, the single-configurational Hartree–Fock function of Eq. (1) is presumably inadequate for considerations of bond-angle and bond-length energetics[27,28] and for descriptions of certain of the low-lying states.[27,28,32] The major inadequacy of the Hartree-Fock description of the O_3 ground state is apparently related to the ionic character of the $1a_2^2$ configuration.[32] This problem does not arise for the $(1a_2^{-1})^2A_2$ hole state,[58] however, and the static-exchange potentials associated with other hole states are expected to be dominated in large measure by the spatial characteristics of the vacated orbital.[50] Consequently, the canonical orbitals should provide ionic hole states that are generally appropriate for studies of the higher excitation spectra and associated photoionization continua in O_3.

Singlet-coupled one-electron excitations of all the occupied orbitals of Eq. (1) are considered here, resulting in excitation/ionization spectra of the forms

$$(6a_1^{-1} ka_1)^1A_1 , \quad (6a_1^{-1} kb_1)^1B_1 , \quad (6a_1^{-1} kb_2)^1B_2 \tag{2a}$$

$$(4b_2^{-1} kb_2)^1A_1 , \quad (4b_2^{-1} ka_1)^1B_1 , \quad (4b_2^{-1} ka_2)^1B_2 \tag{2b}$$

$$(1a_2^{-1} ka_2)^1A_1 , \quad (1a_2^{-1} kb_1)^1B_1 , \quad (1a_2^{-1} kb_2)^1B_2 \tag{2c}$$

$$(1b_1^{-1} kb_1)^1A_1 , \quad (1b_1^{-1} ka_1)^1B_1 , \quad (1b_1^{-1} ka_2)^1B_2 \tag{2d}$$

$$(3b_2^{-1} kb_2)^1A_1 , \quad (3b_2^{-1} ka_1)^1B_1 , \quad (3b_2^{-1} ka_2)^1B_2 \tag{2e}$$

$$(5a_1^{-1} ka_1)^1A_1 , \quad (5a_1^{-1} kb_1)^1B_1 , \quad (5a_1^{-1} kb_2)^1B_2 \tag{2f}$$

$$(4a_1^{-1} ka_1)^1A_1 , \quad (4a_1^{-1} kb_1)^1B_1 , \quad (4a_1^{-1} kb_2)^1B_2 \tag{2g}$$

$$(2b_2^{-1} kb_2)^1A_1 , \quad (2b_2^{-1} ka_1)^1B_1 , \quad (2b_2^{-1} ka_2)^1B_2 \tag{2h}$$

$$(3a_1^{-1} ka_1)^1A_1 , \quad (3a_1^{-1} kb_1)^1B_1 , \quad (3a_1^{-1} kb_2)^1B_2 \tag{2i}$$

$$(2a_1^{-1} ka_1)^1A_1 , \quad (2a_1^{-1} kb_1)^1B_1 , \quad (2a_1^{-1} kb_2)^1B_2 \tag{2j}$$

$$(1b_2^{-1} kb_2)^1A_1 , \quad (1b_2^{-1} ka_1)^1B_1 , \quad (1b_2^{-1} ka_2)^1B_2 \tag{2k}$$

$$(1a_1^{-1} ka_1)^1A_1 , \quad (1a_1^{-1} kb_1)^1B_1 , \quad (1a_1^{-1} kb_2)^1B_2 \tag{2l}$$

corresponding to electric field polarizations in the z (in-plane), x (out-of-plane), and y (in-plane) directions, respectively. It is important to recognize that the one-electron excitation series of Eqs. (2) are not appropriate for descriptions of the low-lying Chappuis, Hartley, and

TABLE I. Supplemental Gaussian basis functions used in O_3 static–exchange calculations.[a]

Location[b]	Type	Number	Exponents[c]
		a_1/a_2	
O_1 and O_2	s/d_{xz}	4/4	0.7 – 0.1/0.6 – 0.1
O_3	$p_x, p_y/p_z$	4,4/4	0.7 – 0.1, 0.7 – 0.1/2.0 – 0.1
O_3	$s/\cdots$	4/$\cdots$	0.15 – 0.025/$\cdots$
O_3	p_y/d_{xz}	4/12	0.1 – 0.0125/1.0 – 0.00156
		b_1/b_2	
O_1 and O_2	$\cdots/s$	$\cdots/3$	$\cdots/1.0 – 0.1$
O_1 and O_2	$p_z/p_x, p_y$	4/3,3	2.0 – 0.1/1.0 – 0.1, 1.0 – 0.1
O_3	p_z/p_x	8/7	2.0 – 0.00156/1.0 – 0.00625

[a]Supplemental basis functions employed, in addition to the $(10s,5p)/[3s,2p]$ valence basis (Ref. 46), in solution of the static–exchange equations [Eqs. (3) to (7)].
[b]O_1 and O_2 refer to the end atoms; O_3 to the central atom.
[c]A geometric series variation is employed in the indicated range when appropriate.

Huggins bands, which apparently involve two-electron transitions in a canonical HF basis.[27,28]

Static-exchange Hamiltonians appropriate for the spectra of Eqs. (2) are constructed in the forms

$$h_\gamma = T + V + V_\gamma , \qquad (3)$$

where T and V are the kinetic- and nuclear-framework potential-energy operators, and

$$V_\gamma = \sum_i (2\hat{J}_i - \hat{K}_i) + \hat{J}_\gamma + \hat{K}_\gamma \qquad (4)$$

is the channel potential, written in terms of Coulomb and exchange operators for the doubly occupied $(\hat{J}_i, \hat{K}_i)$ and singly occupied $(\hat{J}_\gamma, \hat{K}_\gamma)$ orbitals. The resulting non-local, noncentral one-electron Schrödinger equations

$$(h_\gamma - \epsilon) \Phi_{\gamma\epsilon} = 0 , \qquad (5)$$

where ϵ takes on discrete and continuous values, are solved variationally in the forms

$$\langle \widetilde{\Phi}_{\gamma,i} | h_\gamma | \widetilde{\Phi}_{\gamma,j} \rangle = \widetilde{\epsilon}_{\gamma,i} \delta_{ij} , \qquad (6a)$$

$$\langle \widetilde{\Phi}_{\gamma,i} | \widetilde{\Phi}_{\gamma,j} \rangle = \delta_{ij} , \quad i,j = 1, N \qquad (6b)$$

using the virtual canonical orbitals and the supplemental basis sets shown in Table I. The latter are chosen to augment the $(10s, 5p)/[3s, 2p]$ valence basis so that sufficient numbers of compact and diffuse functions are available in each final-state orbital symmetry considered. The combined basis provides pseudospectra [Eqs. (6)] of dimensionalities (N) for the four final-orbital symmetries, $ka_1(26)$, $ka_2(17)$, $kb_1(16)$, and $kb_2(21)$, which are orthogonal to the occupied canonical orbitals of Eq. (1).

Pseudospectra of transition frequencies and oscillators strengths of the dimensionalities indicated above are obtained from Eqs. (1)–(6) in the forms

$$\widetilde{\epsilon}_i^\gamma = \epsilon_\gamma + \widetilde{\epsilon}_{\gamma,i} , \qquad (7a)$$

$$\widetilde{f}_i^\gamma = \tfrac{4}{3} \widetilde{\epsilon}_i^\gamma |\langle \widetilde{\Phi}_{\gamma,i} | \mu | \Phi_\gamma \rangle|^2 , \qquad (7b)$$

where Φ_γ is the appropriate occupied canonical Fock orbital, ϵ_γ is the corresponding Koopmans or experimental ionization potential, μ is the dipole moment operator, and the additional factor of 2 in Eq. (7b) arises from singlet coupling the many-electron eigenstates for the spectra of Eqs. (2). Equations (7) provide transition energies and f numbers for the discrete and autoionizing states lying below the various thresholds and furnish the pseudospectra necessary for the S–T construction of photoionization cross sections above the ionization thresholds. As indicated above, the resulting static-exchange cross sections can be combined with appropriate ionic-state intensity borrowing calculations in order to include the effects of relaxation, and the necessary Franck–Condon factors can also be introduced if the available PES and partial-channel cross section data warrant. These refinements are not included in the present development, but are appropriate subjects for subsequent investigations.

IV. PHOTOEXCITATION AND IONIZATION IN OZONE

A brief qualitative description of the spatial characteristics of the occupied canonical HF symmetry orbitals provides a basis for proper interpretation of the calculated cross sections.[18–25] It will be recalled that $6a_1(n)$ and $4b_2(n)$ are nonbonding/weakly antibonding orbitals, comprised, respectively, of in-phase and out-of-phase combinations of in-plane (yz) end-atom $2p_y$ orbitals, whereas $1a_2(n)$ is nonbonding and comprised of out-of-phase, out-of-plane, end-atom $2p_x$ orbitals. The $1b_1(\pi_x)$ orbital is a π bonding in-phase combination of three out-of-plane $2p_x$ orbitals, $3b_2(n)$ is nonbonding, comprised primarily of end-atom $2s$-$2p$ hybrids, $5a_1(\pi_y)$ is very weakly π_y bonding, $4a_1(\sigma^*)$ is strongly $2s\sigma^*$ antibonding, and $2b_2(\sigma)$ and $3a_1(\sigma)$ are strongly $2s$-$2p\sigma$ and $2s\sigma$ bonding, respectively. The $2a_1(1s)$, $1b_2(1s)$, $1a_1(1s)$ molecular orbitals are appropriate symmetry combinations of $1s$ atomic oxygen orbitals.[18–25] The reader is referred to the literature for more complete descriptions of these orbitals.[18–25]

In addition to the occupied canonical HF symmetry orbitals, $2b_1(\pi_x^*)$, $7a_1(\sigma^*)$, and $5b_2(\sigma^*)$ virtual valence-like orbitals also appear in the ozone spectrum.[18–25] The antibonding $2b_1(\pi_x^*)$ molecular orbital is complementary to the $1b_1(\pi_x)$ bonding orbital, $7a_1(\sigma^*)$ is strongly antibonding and comprised of end- and central-atom $2s$-$2p$ hybrids, and $5b_2(\sigma^*)$ is strongly $2p\sigma^*$ antibonding. The various calculated excitation and ionization spectra should be comprised of intravalence transitions into these relatively compact virtual orbitals, which can appear either above or below the appropriate ionization thresholds, and transitions into more diffuse Rydberg-like discrete and continuum orbitals formed from the supplemental basis set of Table I.

It is convenient in the following to describe and discuss separately the outer-valence-shell ($6a_1$, $4b_2$, $1a_2$), intermediate-valence-shell ($1b_1$, $3b_2$, $5a_1$), inner-valence-shell ($4a_1$, $2b_2$, $3a_1$), and K-edge ($2a_1$, $1b_2$, $1a_1$) cross sections obtained from the present calculations.
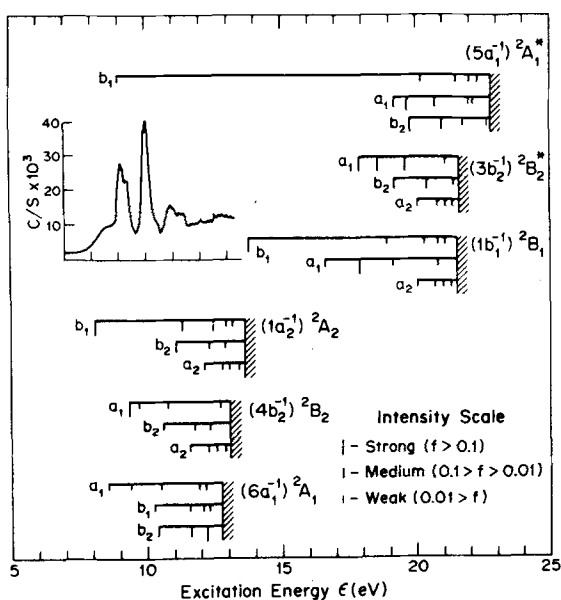
FIG. 1. Improved-virtual-orbital excitation spectra in O_2 obtained from Eqs. (1)–(7) employing the basis sets of Sec. III and and Table I. Numerical values of the transition energies and oscillator strengths are given in Tables II–V. The insert shows the 300 eV electron impact–excitation spectrum (Ref. 15), employing an energy scale identical with that of the overall figures.

A. Outer-valence-shell cross sections

Cross sections for $6a_1(n)$, $4b_2(n)$, and $1a_2(n)$ excitation and ionization are presented in this subsection. Photoelectron spectra indicate the presence of low-lying $^2A_1$, $^2B_2$, and $^2A_2$ states of O_3^* that can be associated with

removal of $6a_1$, $4b_2$, and $1a_2$ canonical orbitals, respectively.[31] Experimental, rather than Koopmans, ionization potentials are employed in the present development to avoid the incorrect ordering predicted by the HF approximation. A semiquantitative description of the calculated outer-valence-shell excitation spectra is given in Fig. 1, in comparison with the measured 300 eV electron impact–excitation profile.[15]

1. $6a_1(n)$ spectra (I.P. = 12.75 eV)

The calculated $6a_1(n) \rightarrow na_1$, nb_1, and nb_2 excitation series are reported and compared with experimental results and quantum-defect estimates in Table II and Fig. 1, and the corresponding $6a_1(n) \rightarrow ka_1$, kb_1, and kb_2 cross sections are shown in Fig. 2(a).

Evidently the $6a_1(n) \rightarrow na_1$ series is comprised of perturbed nsa_1 and npa_1 Rydberg transitions. The basis set employed in a_1 symmetry (Table I) is apparently not large enough to provide separate well-defined nsa_1 and npa_1 Rydberg series. Consequently, agreement with the quantum-defect estimates is only generally satisfactory.[53,54] It should be noted in this connection that the threshold value of the photoionization cross section required in constructing defect estimates of f numbers is generally uncertain by at least a factor of 2 for profiles that are rapidly varying with energy near threshold. Because the series is relatively weak, unique assignment of corresponding features in the impact spectrum of Fig. 1 is not possible. The expected strong $6a_1(n) \rightarrow 7a_1(\sigma^*)$ intravalence transition evidently appears ~ 2 eV above threshold in the $6a_1(n) \rightarrow ka_1$ cross section of Fig. 2(a) as a relatively sharp resonancelike feature.

TABLE II. Outer-valence-shell $6a_1$ (I. P. = 12.75 eV), $4b_2$ (I. P. = 13.03 eV), and $1a_2$ (I. P. = 13.57 eV) excitation spectra in O_3.

Present results[a]	Defect estimates[b]	Present results[a]	Defect estimates[b]	Present results[a]	Defect estimates[b]
energy (eV)/f number	energy (eV)/f number	energy (eV)/f number	energy (eV)/f number	energy (eV)/f number	energy (eV)/f number
$(6a_1)^1A_1 \rightarrow (nsa_1/npa_1)^1A_1$		$(4b_2)^1A_1 \rightarrow (npb_2)^1A_1$		$(1a_2)^1A_1 \rightarrow (nda_2)^1A_1$	
8.54/0.0093	8.98/0.0325	10.57/0.00228	10.5/0.0204	12.13/0.000018	12.1/0.000065
9.38/0.0075	10.2/0.0183	11.73/0.00007	11.8/0.0069	12.76/0.000016	12.7/0.000028
10.50/0.0048	11.1/0.0092	12.31/···	12.3/0.0031	13.03/0.000012	13.0/0.000014
11.92/0.00066	11.5/0.0062	···	···	13.35/···	13.2/0.000008
12.13/0.0019	11.9/0.0038	···	···	···	···
$(6a_1)^1A_1 \rightarrow (npb_1)^1B_1$		$(4b_2)^1A_1 \rightarrow (nda_2)^1B_1$		$(1a_2)^1A_1 \rightarrow (npb_2)^1B_1$	
10.23/0.00048	10.2/0.0018	11.60/0.00099	11.5/0.00202	11.09/0.0140	11.0/0.0161
11.53/0.00015	11.5/0.0005	12.24/0.00051	12.2/0.00085	12.28/0.0018	12.3/0.0023
12.03/0.00006	12.0/0.0003	12.53/0.00030	12.5/0.00044	12.86/0.0017	12.8/0.0010
12.31/0.00006	12.4/0.0001	12.83/···	12.7/0.00025	13.69/···	13.1/0.0005
$(6a_1)^1A_1 \rightarrow (npb_2)^1B_2$		$(4b_2)^1A_1 \rightarrow (nsa_1/npa_1)^1B_2$		$(1a_2)^1A_1 \rightarrow (npb_1)^1B_2$	
10.40/0.0154	10.2/0.0061	9.33/0.1776	9.29/0.0289	8.08/0.9772	···
11.58/0.0295	11.5/0.0021	9.73/0.0049	10.5/0.0163	11.29/0.0529	11.0/0.0246
11.20/0.2206	12.0/0.0009	10.81/0.0007	11.4/0.0081	12.42/0.0106	12.3/0.0083
		12.68/···	11.8/0.0055	12.88/0.0039	12.8/0.0037
				13.16/···	13.1/0.0020

[a]Energies and strengths obtained from the development of Eqs. (1) to (7) and the basis sets described in Sec. III and Table I. The series are made to converge on the experimentally observed vertical photoionization thresholds (Refs. 11–14), as discussed in the text.

[b]Energies taken from the Rydberg formula [$\epsilon_n = \epsilon_t - 13.606/(n - \delta)^2$], and f numbers from the Coulomb-limit approximation [$f_n = g(a. u.)/(n - \delta)^3$] of D. R. Bates and A. Damgaard, Astrophys. J. 242, 14 (1949), and A. Burgess and M. J. Seaton, Mon. Not. R. Astron. Soc. 120, 121 (1960), with $g(a.u.)$ the photoionization oscillator strengths at threshold (Fig. 2). Quantum defects of $\delta = 1.1$, 0.7, and 0 are used for ns, np, and nd series, respectively.
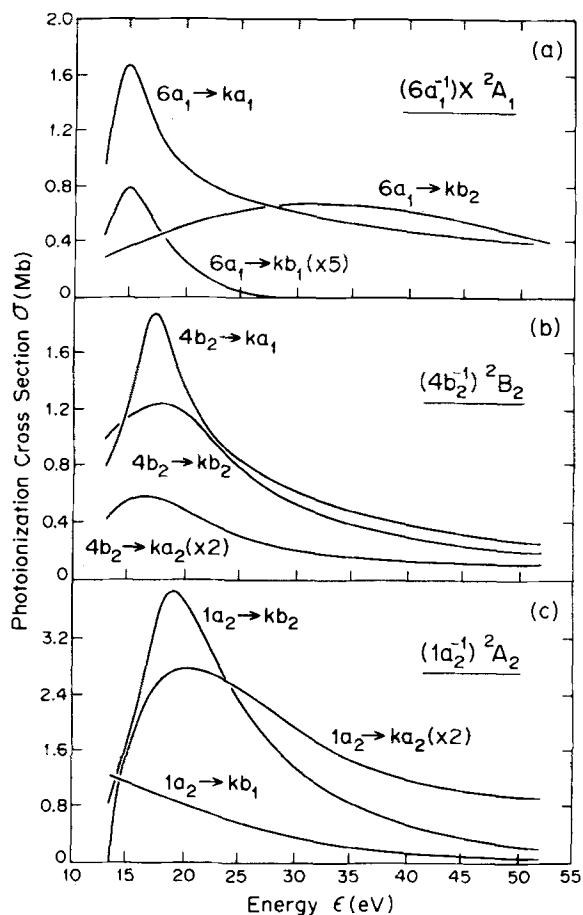
FIG. 2. (a) Calculated S–T static-exchange cross sections in O_3 for $6a_1 \rightarrow ka_1$, kb_1, and kb_2 photoionization obtained from the development of Eqs. (1)–(7). Note that the $6a_1 \rightarrow kb_1$ cross section shown is five times the calculated value. $1 \, Mb = 10^{-18} \, cm^2$. (b) As in (a), for $4b_2 \rightarrow ka_1$, kb_2, and ka_2 photoionization in O_3. The $4b_2 \rightarrow ka_2$ cross section shown is twice the calculated value. (c) As in (a), for $1a_2 \rightarrow kb_2$, ka_2, and kb_1 photoionization in O_3. The $1a_2 \rightarrow ka_2$ cross section shown is twice the calculated value.

The $6a_1 \rightarrow nb_1$ excitations of Table II evidently form a very weak npb_1 Rydberg series, in general agreement with the quantum-defect estimates, although assignments of the impact spectrum are not possible in this case. Similarly, the corresponding $6a_1 \rightarrow kb_1$ photoionization cross section in Fig. 2(a) is also weak, although there is evidence of a $6a_1(n) \rightarrow 2b_1(\pi_x^*)$ resonance-like feature ~ 2 eV above threshold. These results are clarified by noting that $6a_1(n)$ is comprised primarily of in-plane (yz) end-atom $2p_y$ orbitals, whereas npb_1 and kb_1 are primarily of out-of-plane $2p_x$ orbitals.[18–25]

The $6a_1 \rightarrow nb_2$ series of Table II evidently contains a strong intravalence $6a_1(n) \rightarrow 5b_2(\sigma^*)$ interloper in an otherwise npb_2 Rydberg series. Previous experience indicates that the Rydberg-valence interaction in such cases in the static-exchange approximation can be exaggerated and that the correct positions and strengths of the series must be determined by appropriate refined calculations.[42] Consequently, the $6a_1(n) \rightarrow 5b_2(\sigma^*)$ transition may appear in the photoionization continuum or below the Rydberg series members when more elabo-

rate calculations are performed. In the latter case, this intravalence transition could account for the strong feature in the impact spectrum at ~ 10 eV (Fig. 1). Under the assumption that the $6a_1(n) \rightarrow 5b_2(\sigma^*)$ intravalence transition appears below the ionization threshold, the $6a_1 \rightarrow kb_2$ photoionization profile of Fig. 2(a) is determined by deleting the intravalence transition from the imaging procedure. The resulting photoionization profile is evidently generally weak, with a broad maximum at ~ 30 eV.

2. $4b_2(n)$ spectra (I.P. = 13.03 eV)

The $4b_2(n) \rightarrow na_1$, nb_2, and na_2 excitation series are shown in Table II and Fig. 1, and the corresponding $4b_2 \rightarrow ka_1$, kb_2, and ka_2 photoionization cross sections are presented in Fig. 2(b).

Evidently, the $4b_2(n) \rightarrow na_1$ excitations are comprised of perturbed nsa_1 and npa_1 Rydberg series only in general accord with the defect estimates. The relatively strong resonance in the Rydberg series presumably contributes to the sharp line in the experimental spectrum at ~ 9 eV.[15] The expected strong $4b_2(n) \rightarrow 7a_1(\sigma^*)$ intravalence transition apparently appears ~ 5 eV above threshold in the $4b_2 \rightarrow ka_1$ photoionization cross section of Fig. 2(b), similar to the $6a_1 \rightarrow ka_1$ profile of Fig. 2(a). The small difference in peak position in the two profiles can be attributed to differences in detail in the appropriate static-exchange potentials obtained employing many-electron singlet-coupled states.

The $4b_2(n) \rightarrow nb_2$ excitations of Table II evidently comprise a weak npb_2 Rydberg series. In this case, as opposed to the $6a_1(n) \rightarrow nb_2$ series, the $5b_2(\sigma^*)$ valence orbital contributes to the $4b_2 \rightarrow kb_2$ photoionization continuum of Fig. 2(b), resulting in a broad peak ~ 5 eV above threshold.

Finally, the $4b_2(n) \rightarrow nda_2$ Rydberg series is very weak, as might be expected, since $4b_2(n)$ is primarily end atom $2p_y$ in character. The corresponding $4b_2 \rightarrow ka_2$ photoionization cross section of Fig. 2(b) shows evidence of a weak resonancelike structure ~ 4 eV above threshold, however, that can be attributed to atomiclike $2p \rightarrow kd$ contributions to the continuum.

3. $1a_2(n)$ spectra (I.P. = 13.57 eV)

The discrete $1a_2 \rightarrow nb_1$, na_2, and nb_2 excitation series are shown in Table II and Fig. 1, and the corresponding $1a_2 \rightarrow kb_1$, ka_2, and kb_2 cross sections are presented in Fig. 2(c).

A very strong $1a_2(n) \rightarrow 2b_1(\pi_x^*)$ intravalence $n \rightarrow \pi^*$ transition appears in the $1a_1 \rightarrow nb_1$ series, since $1a_2(n)$ is comprised primarily of out-of-plane, out-of-phase, end-atom $2p_x$ orbitals. This transition presumably contributes to the moderately strong and broad feature in the impact spectrum between 8 to 9 eV.[15] The rest of the excitations evidently comprise an npb_1 Rydberg series of moderate intensity, in good accord with the defect estimates. Referring to Fig. 2(c), the $1a_2 \rightarrow kb_1$ photoionization cross section is correspondingly weak, since much of the total f number in this channel appears in the resonance transition.

TABLE III. Intermediate-valence-shell $1b_2$ (I. P. $= 21.51$ eV), $3b_2$ (I. P. $= 21.59$ eV), and $5a_1$ (I. P. $= 22.78$ eV) excitation spectra in in O_3.

Present results[a]	Defect estimates[b]	Present results[a]	Defect estimates[b]	Present results[a]	Defect estimates[b]
energy (eV)/f number	energy (eV)/f number	energy (eV)/f number	energy (eV)/f number	energy (eV)/f number	energy (eV)/f number
$(1b_1)^1A_1 \to (npb_1)^1A_1$		$(3b_2)^1A_1 \to (npb_2)^1A_1$		$(5a_1)^1A_1 \to (nsa_1/npa_1)^1A_1$	
13.85/0.306 2	...	19.23/0.031 1	19.0/0.123	19.26/0.075 1	19.0/0.062 3
18.94/0.0018	18.9/0.0017	20.44/0.016 0	20.4/0.042	19.73/0.126 1	20.3/0.041 1
20.28/0.000 5	20.3/0.000 6	21.42/...	20.8/0.019	20.75/0.061 8	21.2/0.018 5
20.79/0.000 2	20.7/0.000 3	...	...	21.97/0.003 8	21.5/0.013 9
21.07/...	21.0/0.000 1	...	...	22.13/...	21.9/0.007 8
$(1b_1)^1A_1 \to (nsa_1/npa_1)^1B_1$		$(3b_2)^1A_1 \to (nda_2)^1B_1$		$(5a_1)^1A_1 \to (npb_1)^1B_1$	
16.57/0.001 3	17.7/0.068	20.14/0.000 18	20.1/0.000 20	8.99/0.0056	...
17.91/0.113 7	18.9/0.045	20.77/0.000 08	20.8/0.000 09	20.17/0.002 5	20.3/0.004 6
19.13/0.010 0	19.9/0.020	21.06/0.000 04	21.1/0.000 04	21.52/0.000 9	21.5/0.001 6
20.54/0.003 6	20.3/0.016,	21.36/...	21.2/0.000 02	22.04/0.000 4	22.0/0.000 7
20.81/...	20.7/0.009	...	...	22.32/...	22.3/0.000 4
$(1b_1)^1A_1 \to (nda_2)^1B_2$		$(3b_2)^1A_1 \to (nsa_1/npa_1)^1B_2$		$(5a_1)^1A_1 \to (npb_2)^1B_2$	
20.06/0.000 45	20.0/0.000 73	17.87/0.366 6	17.8/0.131 7	19.84/0.141 8	20.3/0.022 4
20.69/0.000 24	20.7/0.000 31	18.59/0.329 6	19.0/0.086 6	20.99/0.056 1	21.5/0.007 6
20.99/0.000 14	21.0/0.000 16	19.61/0.260 2	20.0/0.039 0	21.76/0.006 4	22.0/0.003 4
21.28/...	21.1/0.000 09	21.10/...	20.4/0.029 3	22.71/...	22.3/0.001 8

[a]As in Table II. Koopmans ionization potentials are employed.
[b]As in Table II, employing the threshold oscillator strengths of Fig. 3.

The $1a_2(n) \to nda_2$ Rydberg series is apparently very weak, with the positions in excellent accord with quantum-defect estimates. By contrast, the corresponding $1a_2 \to ka_2$ photoionization profile of Fig. 2(c) shows a very broad atomiclike $2p \to kd$ feature ~ 7 eV above threshold. Similar kd orbital features are predicted and observed in the photoionization spectra of diatomic and other polyatomic molecules having C_{2v} symmetry.[36–45]

The $1a_2(n) \to nb_2$ excitations of Table II evidently form an npb_2 Rydberg series, in very good agreement with the quantum-defect estimates, with no evidence of an intravalence $1a_2(n) \to 5b_2(\sigma^*)$ transition present. The latter feature evidently appears as a resonancelike contribution ~ 6 eV above threshold in the $1a_2 \to kb_2$ photoionization profile of Fig. 2(c), similar to the $4b_2 - kb_2$ profile of Fig. 2(b). By contrast, the $6a_1 \to 5b_2(\sigma^*)$ intravalence transition appears in the discrete position of the $6a_1$ spectrum.

The $1a_2 \to kb_1$, kb_2, and ka_2 photoionization cross sections of Fig. 2(c) and corresponding discrete spectra of Table II are qualitatively similar to the previously reported $1\pi_g$ profiles in molecular oxygen,[40,41] apparently as a consequence of the out-of-plane $2p_x$ character of the $1a_2(n)$ orbital.

B. Intermediate-valence-shell cross sections

The intermediate-valence-shell $1b_1(\pi_x)$, $3b_2(n)$, and $5a_1(\pi_y)$ excitation series are shown in Table III and Fig. 1, and the corresponding photoionization cross sections are given in Fig. 3. Photoelectron spectra indicate weak shakeup lines in the 13.6–17.5 eV interval[10–14] which are not treated here and a stronger line at ~ 20 eV. The latter presumably corresponds to one of the three intermediate-valence-shell orbitals in O_3. Since
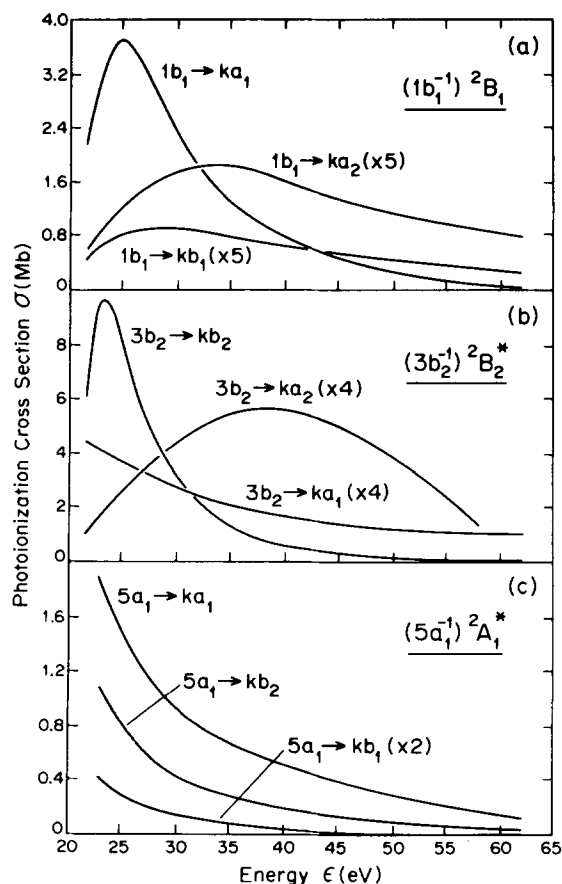

FIG. 3. (a) As in Fig. 2(a), for $1b_1 \to ka_2$, kb_1, and ka_1 photoionization in O_3. The $1b_1 \to ka_2$ and kb_1 cross sections shown are five times the calculated values. (b) As in (a), for $3b_2 \to kb_2$, ka_2, and ka_1 photoionization in O_3. The $3b_2 \to ka_2$ and ka_1 cross sections shown are four times the calculated values. (c) As in (a), for $5a_1 \to ka_1$, kb_2, and kb_1 photoionization in O_3. The $5a_1 \to kb_1$ cross section shown is twice the calculated value.

appropriate experimental values are unavailable, the Koopmans ionization potentials are employed in these cases in the present development.

1. $1b_1(\pi_x)$ spectra (I.P. = 21.51 eV)

The discrete $1b_1(\pi_x) \to na_2$, nb_1, and na_1 excitation series are shown in Table III, and the corresponding $1b_1 \to ka_2$, kb_1, and ka_1 photoionization cross sections are shown in Fig. 3(a).

The $1b_1(\pi_x) \to na_2$ excitations evidently comprise a well-defined nda_2 Rydberg series of weak intensity, in very good agreement with the quantum-defect estimates. Evidently, the corresponding $1b_1 \to ka_2$ cross section of Fig. 3(a) contains a broad but very weak kda_2 feature at ~ 32 eV, in accord with the $4b_2 \to ka_2$ and $1a_2 \to ka_2$ profiles of Figs. 2(b) and 2(c), respectively. Apparently, the out-of-plane $2p_x$ character of the $1b_1(\pi_x)$ orbital is inappropriate for the formation of strong overlap charge with the na_2/ka_2 spectrum.

As expected, there is a strong $1b_1(\pi_x) \to 2b_1(\pi_x^*)$ $\pi \to \pi^*$ transition in the $1b_1 \to nb_1$ series, with the other members comprising a well-defined npb_1 Rydberg series. The associated $1b_1 \to kb_1$ photoionization cross section of Fig. 3(a) is correspondingly weak, similar to the structures of previously reported $\pi \to k\pi^*$ channels in diatomic molecules.[36-42]

Finally, the $1b_1(\pi_x) \to na_1$ excitations evidently form perturbed nsa_1 and npa_1 Rydberg series, and the corresponding $1b_1 \to ka_1$ photoionization cross section contains a strong $1b_1(\pi_x) \to 7a_1(\sigma^*)$ resonancelike contribution immediately above threshold.

2. $3b_2(n)$ spectra (I.P. = 21.59 eV)

The discrete $3b_2(n) \to na_1$, nb_2, and na_2 series are shown in Table III and Fig. 1, and the corresponding ka_1, kb_2, and ka_2 cross sections are given in Fig. 3(b).

Evidently, the $3b_2(n) \to na_1$ excitations of Table III form strong nsa_1 and npa_1 Rydberg series, perturbed by a $3b_2(n) \to 7a_1(\sigma^*)$ intravalence interloper, and the $3b_2(n) \to ka_1$ photoionization cross section is correspondingly weak and monotonic. By contrast, the $4b_2 \to na_1/ka_1$ profile [Table II and Fig. 2(b)] exhibits a $7a_1(\sigma^*)$ photoionization resonance. Calculations somewhat more elaborate than the static-exchange results reported here are required to confirm the positioning of the $3b_2(n) \to 7a_1(\sigma^*)$ transition in the discrete spectrum, since the positions of intravalence transitions can be sensitive to the details of configuration interaction.[42]

The $3b_2(n) \to nb_2$ excitations of Table III form a reasonably well-defined, moderate intensity, npb_2 Rydberg series, whereas the corresponding $3b_2(n) \to kb_2$ cross section of Fig. 3(b) has a strong $3b_2(n) \to 5b_2(\sigma^*)$ resonance ~ 1.5 eV above threshold. The latter is the strongest individual feature present in the O_3 photoionization cross section. It can be attributed to the strong $\sigma \to \sigma^*$ like transition density arising from the $3b_2(n) \cdot 5b_2(\sigma^*)$ product and is qualitatively similar to the $3\sigma_g \to k\sigma_u$ resonance in molecular oxygen.[40,41]

Finally, the $3b_2(n) \to na_2$ excitations of Table III comprise a well-defined but very weak nda_2 Rydberg series, in excellent agreement with the quantum-defect estimates. The corresponding $3b_2(n) \to ka_2$ photoionization cross section of Fig. 3(b) is weak, but shows clear evidence of a broad kd atomiclike contribution, peaking at somewhat higher energy than in the $1b_1(\pi_x) \to ka_2$ profile of Fig. 3(a).

3. $5a_1(\pi_y)$ spectra (I.P. = 22.78 eV)

The $5a_1(\pi_y) \to na_1$, nb_1, and nb_2 excitation series are shown in Table III and Fig. 1, and the corresponding ka_1, kb_1, and kb_2 cross sections are given in Fig. 3(c).

The $5a_1(\pi_y) \to na_1$ excitations evidently form perturbed nsa_1 and npa_1 Rydberg series of moderate intensity, and the ka_1 cross section of Fig. 3(c) is monotonically decreasing. There is little evidence in this channel of a $5a_1 \to 7a_1(\sigma^*)$ resonance contribution in either the discrete or continuous spectral regions, although this feature may be mixed in the perturbed Rydberg series. The π_y character of the $5a_1$ orbital is apparently inappropriate for forming a strong transition charge density with the $7a_1(\sigma^*)$ virtual valence orbital.

Although the $5a_1(\pi_y) \to nb_1$ series contains an intravalence transition, its intensity is apparently quite weak, as may be expected from the out-of-plane character of the $2b_1(\pi_x^*)$ orbital. The other $5a_1 \to nb_1$ excitations evidently form a weak npb_1 Rydberg series, in good agreement with the quantum-defect estimates. The associated $5a_1 \to kb_1$ photoionization cross section of Fig. 3(c) is correspondingly weak and monotonically decreasing, presumably also as a consequence of the out-of-plane character of the kb_1 orbitals.

Finally, the $5a_1 \to nb_2$ excitations of Table III form an npb_2 Rydberg series of moderate intensity, with little indication of an intravalence $5a_1(\pi_y) \to 5b_2(\sigma^*)$ present in either the discrete spectrum or the $5a_1 \to ka_1$ cross section of Fig. 3(c), although it may contribute to the resonance transition. Apparently the directions of the $5b_2(\sigma^*)$ hybrid lobes are such that a strong overlap charge density is not formed with the $5a_1(\pi_y)$ orbital.

C. Inner-valence-shell cross sections

The inner-valence-shell $4a_1(\sigma^*)$, $2b_2(\sigma)$, and the $3a_1(\sigma)$ excitation spectra are shown in Table IV, and corresponding photoionization cross sections appear in Fig. 4. Koopmans values are employed in the absence of experimentally determined vertical ionization potentials. Because of strong configuration mixing in the inner-valence-shell ionic states of molecules containing first row atoms,[52] the results of Fig. 4 should be combined with appropriate intensity borrowing calculations prior to making comparison with experiment.

1. $4a_1(\sigma^*)$ spectra (I.P. = 29.86 eV)

The $4a_1(\sigma^*) \to nsa_1$ and npa_1 Rydberg series of Table IV is irregular and weak, and the positions are only in fair agreement with the quantum-defect estimates, apparently due to limitations of the basis set of Table I. The as-

TABLE IV. Inner-valence-shell $4a_1$ (I. P. = 29.9 eV), $2b_2$ (I P. = 39.6 eV), and $3a_1$ (I. P. = 48.6 eV) excitation spectra in O_3.

Present results[a]	Defect estimates[b]	Present results[a]	Defect estimates[b]	Present results[a]	Defect estimates[b]
energy (eV)/f number	energy (eV)/f number	energy (eV)/f number	energy (eV)/f number	energy (eV)/f number	energy (eV)/f number
$(4a_1)^1A_1 \rightarrow (nsa_1/npa_1)^1A_1$		$(2b_2)^1A_1 \rightarrow (npb_2)^1A_1$		$(3a_1)^1A_1 \rightarrow (nsa_1/npa_1)^1A_1$	
26.24/0.007 60	26.1/0.008 5	37.20/0.004 0	37.0/0.004 1	44.62/0.005 5	44.8/0.008 5
26.59/10⁻⁷	27.3/0.005 6	38.40/0.004 2	38.3/0.001 4	44.94/0.001 4	46.0/0.005 6
27.56/0.000 26	28.2/0.002 5	39.20/0.021 8	38.8/0.000 6	46.16/0.002 1	46.9/0.002 5
28.96/0.000 25	28.6/0.001 9	...	...	47.57/0.000 9	47.3/0.001 9
29.22/...	29.0/0.001 1	...	...	47.70/...	47.7/0.001 1
$(4a_1)^1A_1 \rightarrow (npb_1)^1B_1$		$(2b_2)^1A_1 \rightarrow (nda_2)^1B_1$		$(3a_1)^1A_1 \rightarrow (npb_1)^1B_1$	
18.41/0.339 4	...	38.12/10⁻⁶	38.1/10⁻⁶	34.59/...	...
27.21/0.000 49	27.3/0.000 45	38.76/...	38.7/...	45.85/0.000 65	46.0/0.000 9
28.62/0.000 15	28.6/0.000 15	39.06/...	39.0/...	47.27/0.000 30	47.3/0.000 3
29.13/0.000 07	29.1/0.000 07	39.35/...	39.2/...	47.80/0.000 15	47.8/0.000 1
29.41/...	29.4/0.000 04	...	...	48.08/...	48.1/0.000 1
$(4a_1)^1A_1 \rightarrow (npb_2)^1B_1$		$(2b_2)^1A_1 \rightarrow (nsa_1/npa_1)^1B_2$		$(3a_1)^1A_1 \rightarrow (npb_2)^1B_2$	
27.42/0.000 69	27.3/0.006 1	35.60/0.041 8	35.8/0.012 4	45.46/0.013 0	...
28.61/0.000 98	28.6/0.002 1	36.19/0.007 3	37.0/0.008 2	46.59/0.011 7	46.0/0.008 1
29.27/0.005 2	29.1/0.000 9	37.29/0.002 9	38.0/0.003 7	47.48/0.003 1	47.3/0.002 7
		39.10/...	38.3/0.002 8	48.43/0.002 7	47.8/0.001 2

[a]As in Table II. Koopmans ionization potentials are employed.
[b]As in Table II, employing the threshold oscillator strengths of Fig. 4.

sociated $4a_1 \rightarrow ka_1$ cross section of Fig. 4(a) is also correspondingly weak, although there is evidence of a broad $7a_1(\sigma^*)$ resonance present, centered at ~55 eV. By contrast, the $4a_1 \rightarrow nb_1$ series contains a relatively strong $4a_1(\sigma^*) \rightarrow 2b_1(\pi_y^*)$ intravalence transition, and the associated $4a_1 \rightarrow kb_1$ continuum goes to zero at threshold. Finally, the $4a_1 \rightarrow nb_2$ excitations constitute an npb_2 Rydberg series in general agreement with defect estimates, and there is a definite $4a_1 \rightarrow 5b_2(\sigma^*)$ resonance present in the kb_2 continuum centered at ~50 eV. All three cross sections are evidently less than 1 Mb in value for all energy.

2. $2b_2(\sigma)$ spectra (I.P. = 39.58 eV)

The $2b_2(\sigma) \rightarrow nb_2$ series of Table IV is evidently a weak npb_2 Rydberg series, apparently perturbed by the $5b_2(\sigma^*)$ resonance just below threshold, similar to the $6a_1 \rightarrow nb_2$ series of Table II and Fig. 1. Since this feature appears above threshold in the $4b_2 \rightarrow kb_2$ [Fig. 2(b)] and $3b_2 \rightarrow kb_2$ [Fig. 3(b)] cross sections, refined calculations would seem to be in order to further clarify its location.[42] The $2b_2 \rightarrow kb_2$ cross section of Fig. 4(a) has been constructed by deleting the $2b_2 \rightarrow 5b_2(\sigma^*)$ contribution from the spectrum in the imaging procedure.

The $2b_2(\sigma) \rightarrow nda_2$ Rydberg series of Table IV is evidently extremely weak, although the $2b_2 \rightarrow ka_2$ cross section of Fig. 4(b) shows a definite resonancelike structure at ~60 eV. This is presumably a consequence of kd contributions, familiar from other investigations.[43–45]

Finally, the $2b_2(\sigma) \rightarrow nsa_1/npa_1$ Rydberg series is irregular and perturbed by the $7a_1(\sigma^*)$ resonance below threshold, similar to the $3b_2 \rightarrow na_1/ka_1$ profile of Table III and Fig. 3(b). By contrast, the $4b_2 \rightarrow ka_1$ cross section of Fig. 2(b) has a well defined $7a_1(\sigma^*)$ resonance above threshold. Evidently, the $2b_2 \rightarrow ka_1$ and $2b_2 \rightarrow kb_2$ cross sections approach a common limit at high energy.

3. $3a_1(\sigma)$ spectra (I.P. = 48.55 eV)

Evidently, the $3a_1(\sigma) \rightarrow na_1$ excitations of Table IV comprise weak nsa_1 and npa_1 Rydberg series, whereas
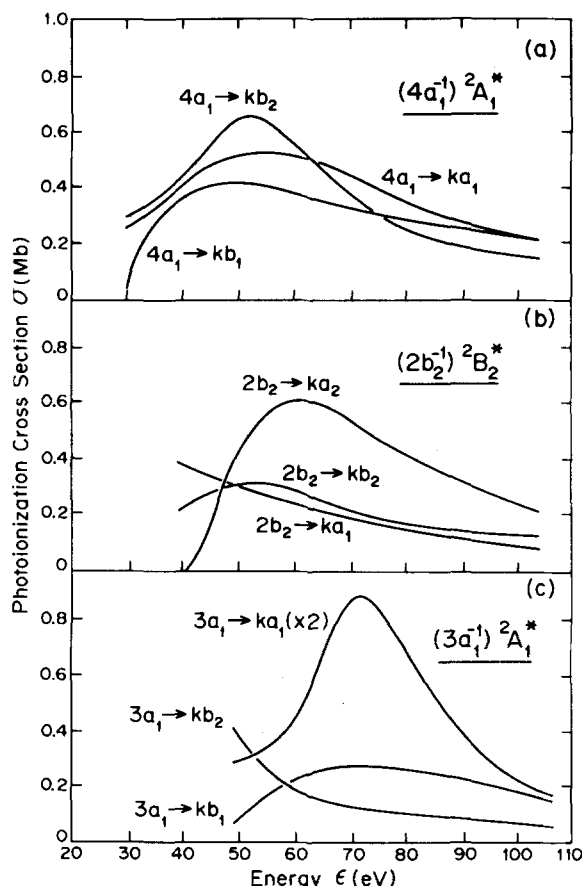

FIG. 4. (a) As in Fig. 2(a), for $4a_1 \rightarrow ka_1$, kb_2, and kb_1 photoionization in O_3. (b) As in (a), for $2b_2 \rightarrow kb_2$, ka_2, and ka_1 photoionization in O_3. (c) As in (a), for $3a_1 \rightarrow ka_1$, kb_2, and kb_1 photoionization in O_3. The $3a_1 \rightarrow ka_1$ cross section shown is twice the calculated value.

there is a strong intravalence $3a_1(\sigma) \to 7a_1(\sigma^*)(\sigma \to \sigma^*)$ contribution to the ka_1 continuum of Fig. 4(c) at ~ 70 eV. The $3a_1 \to nb_2$ excitations comprise a weak Rydberg series, with a moderately strong $3a_1(\sigma) \to 5b_2(\sigma^*)(\sigma \to \sigma^*)$ transition also present. The kb_2 continuum is correspondingly weak and monotonically decreasing. Finally, there is a weak low-lying $3a_1(\sigma) \to 2b_1(\pi_x^*)$ transition in the $3a_1 \to nb_1$ excitations and a weak Rydberg series, and the corresponding kb_1 continuum shows a broad maximum at ~ 70 eV.

D. Valence shell partial-channel cross sections

The various polarization components of the partial-channel cross sections of Figs. 2–4 are combined and presented in Fig. 5. Of the three low ionization potential nonbonding orbitals ($6a_1$, $4b_2$, $1a_2$), the $1a_2$ orbital evidently makes the major contribution to the photoionization cross sections shown in Fig. 5(a). The peak at ~ 20 eV in this partial-channel profile is due to $1a_2(n) \to 5b_2(\sigma^*)$ and $1a_2(n) \to a_2 kd$ resonancelike contributions [Fig. 2(c)] to the $1a_2(n) \to kb_2$ and ka_2 components. As indicated above, the $1a_2(n)$ cross sections are qualitatively similar to the previously reported $1\pi_g^{-1}$ results in molecular oxygen,[40,41] apparently as a consequence of the out-of-plane $2p_x$ character of the $1a_2(n)$ orbital. Although the $6a_1$ and $4b_2$ partial-channel cross sections are weaker, there is evidence of a $6a_1(n) \to 7a_1(\sigma^*)$ resonance contribution in the former [Fig. 2(a)], and $4b_2(n) \to 7a_1(\sigma^*)$ $5b_2(\sigma^*)$, and $a_2 kd$ resonances in the latter [Fig. 2(b)]. The $6a_1(n)$ and $4b_2(n)$ results are qualitatively similar to the $1\pi_u$ and $1\pi_g$ cross sections in O_2,[40,41] although less so than in the case of the $1a_2(n)$ orbital indicated above, presumably as a consequence of the in-plane $2p_y$ character of the $6a_1(n)$ and $4b_2(n)$ orbitals. In order to separate the three partial cross sections of Fig. 5(a) for parent O_3^+ ion formation into vibrationally bound and dissociative components, appropriate potential surfaces and Franck-Condon factors must be constructed. These aspects of photoionization in O_3 are beyond the scope of the present investigation.

In the spectral interval from ~ 13 to 21 eV there are a series of discrete excitations associated with intravalence and Rydberg transitions converging to the higher ionization thresholds at ~ 21 to 22 eV (Fig. 1 and Table III). These excitations can autoionize into the underlying $6a_1$, $4b_2$, and $1a_2$ photoionization continua, and appropriate line-shape calculations are required to obtain the correct intensity distribution in the 13–21 eV interval. In the absence of these calculations, estimates of the ionization cross section are obtained by including in the S–T analysis all the discrete f numbers of Table III. The profile so obtained corresponds approximately to total ionization from these states, and so gives an upper limit. By contrast, the direct ionization curves for $6a_1$, $4b_2$, and $1a_2$ orbitals provide a lower estimate of the one-electron ionization contribute to the photoabsorption cross section in the ~ 13–21 eV interval.

Above ~ 21 eV the $1b_1$, $3b_2$, and $5a_1$ partial-channel cross sections shown in Fig. 5(b) contribute to O_3^+ parent ion formation. Evidently, the $3b_2$ contribution dominates in this spectral region, due to the $3b_2(n) \to 5b_2(\sigma^*)$ reso-
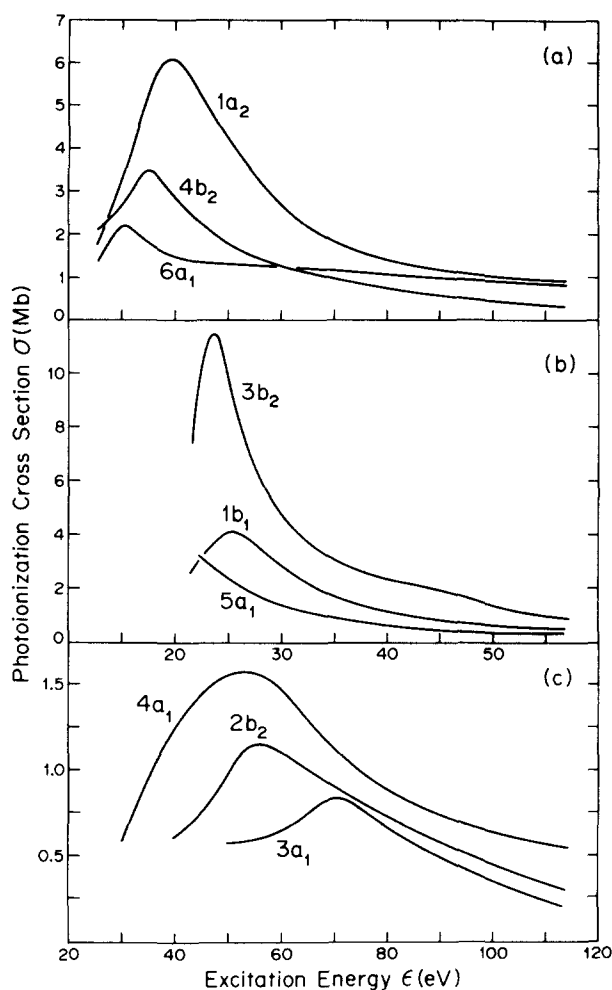

FIG. 5. (a) Outer-valence-shell $6a_1$, $4b_2$, and $1a_2$ partial-channel photoionization cross sections in O_3 obtained from Fig. 2. (b) As in (a), for $1b_1$, $3b_2$, and $5a_1$ photoionization in O_3 from Fig. 3. (c) As in (a), for $4a_1$, $2b_2$, and $3a_1$ photoionization in O_3 from Fig. 4. Note that the energy scale in this case differs from that of (a) and (b).

nance at ~ 23 eV in the $3b_2 \to kb_2$ photoionization cross section [Fig. 3(b)]. As indicated above, this feature corresponds closely to the strong $\sigma \to \sigma^*$ resonancelike contribution just above threshold in the $3\sigma_g \to k\sigma_u$ photoionization cross section in molecular oxygen.[40,41] Although the $1b_1$ cross section is smaller in magnitude, the $1b_1(\pi_x) \to 7a_1(\sigma^*)$ resonancelike contribution to this channel [Fig. 3(a)] is apparent in the partial cross section of Fig. 5(b). Finally, the $5a_1$ cross section of Fig. 5(b) is generally weak and monotonic, apparently as a consequence, as indicated previously, of the out-of-plane π_y character of this orbital, which prevents formation of strong overlap densities with the valencelike virtual orbitals. The total calculated photoionization cross section in the ~ 22–30 eV interval is seen to be monotonic and structureless, in general accord with photoabsorption[4–10] and electron-impact[15] measurements.

With the exception of the strong intravalence $4a_1(\sigma^*)$ $\to 2b_1(\pi_x^*)$ transition, the discrete transitions of Table IV arising from inner-valence-shell excitation are seen to be relatively weak. Consequently, the total photoionization cross section will be generally structureless up to

TABLE V. K-edge $2a_1$ (I.P. =541.5 eV), $1b_2$ (I.P. =541.5 eV), and $1a_1$ (I.P. =546.2 eV) excitation spectra in O_3.

Present results[a]	Defect estimates[b]	Present results[a]	Defect estimates[b]	Present results[a]	Defect estimates[b]
energy (eV)/f number	energy (eV)/f number	energy (eV)/f number	energy (eV)/f number	energy (eV)/f number	energy (eV)/f number
$(2a_1)^1A_1\rightarrow (nsa_1/npa_1)^1A_1$		$(1b_2)^1A_1\rightarrow (npb_2)^1A_1$		$(1a_1)^1A_1\rightarrow (nsa_2/npa_1)^1A_1$	
532.3/0.013 4	...	536.5/0.036 86	...	534.8/0.050 0	...
538.0/0.001 0	538.1/0.005 0	539.3/0.000 60	539.0/0.005 1	541.6/0.003 4	542.9/0.006 9
539.1/0.002 8	539.0/0.003 3	540.4.0.000 02	540.5/0.001 7	543.7/0.000 8	543.7/0.004 5
540.5/0.002 3	540.0/0.001 5	541.4/...	540.8/0.000 8	544.8/0.002 2	544.7/0.002 0
540.8/...	540.5/0.001 1	...	541.1/0.000 4	545.3/...	545.0/0.001 5
$(2a_1)^1A_1\rightarrow (npb_1)^1B_1$		$(1b_2)^1A_1\rightarrow (nda_2)^1B_1$		$(1a_1)^1A_1\rightarrow (npb_1)^1B_1$	
524.5/0.090 3	...	540.0/0.001 15	540.0/0.001 48	524.1/0.092 4	...
538.9/0.001 9	539.0/0.001 8	540.7/0/000 57	540.7/0.000 63	543.3/0.001 6	543.7/0.002 9
540.3/0.000 6	540.5/0.000 6	541.0/0.000 32	541.0/0.000 32	544.9/0.000 9	545.0/0.001 0
540.8/0.000 3	540.8/0.000 3	541.3/...	541.2/0.000 19	545.4/0.000 4	545.5/0.000 4
541.1/0.000 2	541.1/0.000 2	...	541.3/0.000 12	545.7/0.000 3	545.8/0.000 2
$(2a_1)^1A_1\rightarrow (npb_2)^1B_2$		$(1b_2)^1A_1\rightarrow (nsa_1/npa_1)^1B_2$		$(1a_1)^1A_1\rightarrow (npb_2)^1B_2$	
536.5/0.037 6	...	532.3/0.087 7	...	533.7/0.112 0	...
539.3/0.005 4	539.0/0.006 8	538.0/0.000 2	538.1/0.010 9	543.9/0.000 5	543.7/0.000 7
540.4/0.001 6	540.5/0.002 3	539.1/...	539.0/0.007 2	545.1/0.000 2	545.2/0.000 2
541.4/...	540.8/0.001 0	540.9/...	540.0/0.003	546.0/...	545.5/0.000 1

[a]As in Table II, employing experimentally determined ionization potentials (Ref. 59).
[b]As in Table II, employing the threshold oscillator strengths of Fig. 6.

the ~ 30 eV threshold for $4a_1$ ionization. The partial-channel cross sections for $4a_1$, $2b_2$, and $3a_1$ ionization shown in Fig. 5(c) are evidently weak, although their combined peaks may be evident in the total cross section. Apparently the $4a_1$ contribution is the largest of the three inner-valence-shell cross sections shown in Fig. 5(c), a consequence of the $4a_1(\sigma^*)$ and $7a_1(\sigma^*)$ resonances in this case [Fig. 4(a)]. The prominent features in the $2b_2$ and $3a_1$ cross sections of Fig. 5(c) are due to $2b_2(\sigma)\rightarrow ka_2d$ [Fig. 4(b)] and $3a_1(\sigma)\rightarrow 7a_1(\sigma^*)$ [Fig. 4(c)] resonances, respectively. These features are similar to resonancelike structures appearing in the inner-valence-shell $2\sigma_u$ and $2\sigma_g$ cross sections in molecular oxygen. Of course it should be noted, as indicated above, that the Koopmans approximation generally fails in the inner-valence-shell ionization spectrum of molecules containing first row atoms.[52] Consequently, the results of Fig. 5(c) must be combined with appropriate ionic-state amplitudes prior to making comparison with experiment.

E. K-edge cross sections

The K-edge $2a_1$, $1b_2$, and $1a_1$ excitation series are shown in Table V, and the corresponding photoionization cross sections are shown in Fig. 6. Experimental ionization potentials are employed in these three cases.[59] These values are in general accord with other oxygen atom $1s$ ionization thresholds reported in the ~ 530–545 eV interval in various oxygen containing compounds.[60] The $1a_1$ molecular orbital corresponds essentially to a central oxygen atom $1s$ orbital, whereas the degenerate $2a_1$ and $1b_2$ molecular orbitals correspond to appropriate even and odd combinations of end-atom $1s$ orbitals, respectively.

1. $2a_1$ spectra (I.P. =541.5 eV)

The $2a_1\rightarrow na_1$ series of Table V evidently contains a strong transition into the $7a_1(\sigma^*)$ orbital and interacting

nsa_1 and npa_1 Rydberg series, and the corresponding $2a_1 \rightarrow ka_1$ cross section is a broad weak continuum [Fig. 6(a)]. Similarly, the $2a_1 \rightarrow npb_1$ series contains a very
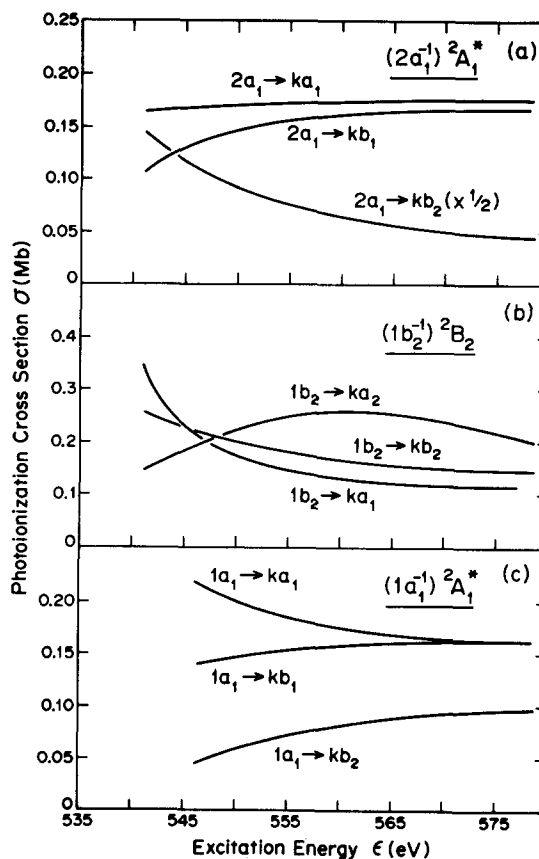

FIG. 6. (a) As in Fig. 2(a), for $2a_1\rightarrow ka_1$, kb_1, and kb_2 photoionization in O_3. (b) As in (a), for $1b_2\rightarrow kb_2$, ka_1, and ka_2 photoionization in O_3. (c) As in (a), for $1a_1\rightarrow ka_1$, kb_1, and kb_2 photoionization in O_3.

strong transition into the $2b_1(\pi_x^*)$ valencelike orbital, and a weak Rydberg series in good accord with quantum-defect estimates. The $2a_1 \rightarrow kb_1$ photoionization continuum of Fig. 6(a) is correspondingly weak and structureless. The $2a_1 \rightarrow npb_2$ series of Table V evidently contains a moderately strong transition into the $5b_2(\sigma^*)$ orbital, and a Rydberg series in good accord with quantum-defect estimates. The corresponding continuum cross section of Fig. 6(a) is relatively weak, although the increase near threshold is in accord with recent measurements of the K-edge cross section in O_2.[61] Moreover, the strong $2a_1 \rightarrow 2b_1(\pi_x^*)$ transition well below threshold corresponds to the observed intense $1\sigma_u - 1\pi_g$ excitation in O_2, and the $2a_1 \rightarrow 5b_2(\sigma^*)$ transition close to threshold is in accord with a strong feature in the O_2 spectrum just below threshold that can be given a $1\sigma_g - 2p\sigma_u$ assignment.[61] By contrast, the $2a_1 \rightarrow 7a_1(\sigma^*)$ valencelike resonance does not have a counterpart in the O_2 K-edge spectra.

2. $1b_2$ spectra (I.P. = 541.5 eV)

The $1b_2 \rightarrow npb_2$ series of Table V evidently contains a strong resonance transition associated with the $5b_2(\sigma^*)$ orbital, whereas the corresponding cross section of Fig. 6(b) is monotonic and structureless. The positions of the other members of the $1b_2 \rightarrow npb_2$ series are evidently in good agreement with quantum-defect estimates, and the f numbers are relatively weak. Note that the $1b_2 \rightarrow 5b_2(\sigma^*)$ resonance is degenerate with the corresponding $2a_1 \rightarrow 5b_2(\sigma^*)$ transition discussed above. Presumably localized $1s$ end-oxygen-atom orbital calculations in ozone, including relaxation effects, will aid in refining the position of these features, which are expected to appear just below threshold on basis of the measurements in O_2.[61] The $1b_2 \rightarrow na_1$ excitations of Table V form separate nsa_1 and npa_1 Rydberg series, although the basis set is apparently insufficient to resolve them completely. Moreover, the resonance transition into the $7a_1(\sigma^*)$ valencelike orbital is degenerate with the $2a_1 \rightarrow 7a_1(\sigma^*)$ excitation indicated above, suggesting that localized-orbital calculations including relaxation are in order. The corresponding $1b_2 \rightarrow ka_1$ photoionization cross section shown in Fig. 6(b) is rapidly increasing at threshold, in accord with recent measurements in O_2.[61] Finally, the $1b_2 \rightarrow na_2$ excitations evidently comprise a weak Rydberg series, and the associated photoionization continuum apparently exhibits an a_2kd resonancelike broad maximum.

3. $1a_1$ spectra (I.P. = 546.2 eV)

The $1a_1 \rightarrow nb_2$ series of Table V evidently contains a strong $1a_1 \rightarrow 5b_2(\sigma^*)$ transition and a very weak $1a_1 \rightarrow npb_2$ Rydberg series, with a correspondingly weak unstructured photoionization continuum [Fig. 6(c)]. As in the $2a_1 \rightarrow na_1$ series, there is a strong $1a_1 \rightarrow 7a_1(\sigma^*)$ resonance in the $1a_1 \rightarrow na_1$ series of Table V and also interacting nsa_1/npa_1 Rydberg series, the positions of which are in general accord with defect estimates. In this case the photoionization continuum of Fig. 6(c) is slightly increasing near threshold. The $1a_1 \rightarrow npb_1/kb_1$ spectrum of Table V and Fig. 6(c) is evidently highly similar to that of the $2a_1$ orbital. Because the $1a_1$ transitions into the valencelike $5b_2(\sigma^*)$, $7a_1(\sigma^*)$, and $2b_1(\pi_x^*)$ virtual

orbitals are not degenerate with the corresponding $2a_2$ and $1b_2$ excitations, the K-edge spectrum in O_3 below threshold will be more structured than that in O_2.[61]

V. CONCLUDING REMARKS

The present studies provide an overall account of the vertical dipole excitation/ionization spectrum in molecular ozone in the IVO–static-exchange approximation. Use of the Stieltjes–Tchebycheff technique and conventional bound-state computational methods allows for discussion and clarification of the resulting discrete and continuous spectra on a common basis using familar molecular-orbital concepts. It is found that the various excitation and ionization spectra can be understood in terms of contributions from valencelike virtual $2b_1(\pi_x^*)$, $5b_2(\sigma^*)$, and $7a_1(\sigma^*)$ orbitals and from more diffuse Rydberg-like orbitals. In addition, there is also evidence of contributions in ka_2 final-state symmetry from kd atomiclike orbitals. Similar interpretations have also been employed previously in studies of diatomic and other polyatomic molecules.

Certain of the partial-channel photoexcitation/ionization cross sections in ozone are qualitatively similar to previously reported results in molecular oxygen. The $1a_2(n)$ and $1b_1(\pi_x)$ cross sections, in particular, are highly similar to $1\pi_g$ and $1\pi_u$ results in molecular oxygen, respectively, apparently as a consequence of the out-of-plane $2p_x$ character of the $1a_2$ and $1b_1$ molecular orbitals. There are also similarities between the $6a_1(n)$ and $4b_2(n)$ cross sections in ozone and the $1\pi_u$ and $1\pi_g$ channels in O_2, respectively. The similarity is less precise in these cases than it is for the $1a_2(n)$ and $1b_1(\pi_x)$ orbitals, however, apparently as a consequence of the largely in-plane $2p_y$ character of the $6a_1$ and $4b_2$ canonical orbitals. Most striking, however, is the strong $\sigma \rightarrow \sigma^*$ resonance in the $3b_2 \rightarrow kb_2$ channel, which is in qualitative accord with a closely related $\sigma \rightarrow \sigma^*$ feature in the molecular oxygen $3\sigma_g \rightarrow k\sigma_u$ cross section. The calculated K-edge spectra in O_3 also show similarities to recent photoabsorption cross-section measurements in O_2.

Although the results reported here are in accord with electron impact–excitation spectra and with general expectations, experimental partial-channel photoionization cross sections are not available for comparison at present. Of course, it will be necessary to combine the static-exchange cross sections with the results of intensity-borrowing ionic-state and Franck–Condon calculations prior to making detailed comparison with measured partial-channel cross sections, particularly in the inner-valence-shell region of the spectrum. In order to independently assess the reliability of the outer-valence-shell cross sections, which should be largely independent of the effects of shakeup in the ionic cores, it will be desirable to make comparisons with static-exchange cross sections based on ionization of more localized GVB orbitals, which can provide an appropriate description of the biradical character of ground state ozone. Similarly, it will also be helpful to compare in the K-edge region photoionization calculations employing relaxed localized hole states, rather than the symmetry orbitals employed in the present development. Furthermore, because static-exchange calcula-

tions can give incorrect positionings of compact intra-valence transitions in certain cases, it will also be desirable to investigate the effects of configuration mixing in this connection. These topics are investigated separately in subsequent papers.

ACKNOWLEDGMENTS

[1] Critical Review of Ultraviolet Photoabsorption Cross Sections for Molecules of Astrophysical and Aeronomic Interest, edited by R. D. Hudson, NSRDS-NBS 38 (U.S. GPO, Washington, D. C., 1971).

[2] G. Herzberg, Electronic Spectra of Polyatomic Molecules (Van Nostrand, Princeton, 1966), p. 511.

[3] E. Lissi and J. Heicklen, J. Photochem. 1, 39 (1972); J. R. Peterson, J. Geophys. Res. 81, 1433 (1976).

[4] W. C. Price and D. M. Simpson, Trans. Faraday Soc. 37, 106 (1941).

[5] Y. Tanaka, E. C. Y. Inn, and K. Watanabe, J. Chem. Phys. 21, 1651 (1953).

[6] M. Ogawa and G. R. Cook, J. Chem. Phys. 28, 173 (1958).

[7] M. Griggs, J. Chem. Phys. 49, 857 (1968).

[8] J. W. Simons, R. J. Paur, H. A. Webster III, and E. J. Bair, J. Chem. Phys. 59, 1203 (1973).

[9] A. Devagnet and J. Ryan, Chem. Phys. Lett. 22, 269 (1973).

[10] D. Grimbert and A. Davagnet, Mol. Phys. 27, 831 (1974).

[11] D. W. Turner, C. Baker, A. D. Baker, and C. R. Brundle, Molecular Photoelectron Spectroscopy (Wiley, New York, 1970); T. N. Radwan and D. W. Turner, J. Chem. Soc. A 1966, 85.

[12] D. C. Frost, S. T. Lee, and C. A. McDowell, Chem. Phys. Lett. 24, 149 (1972).

[13] C. R. Brundle, Chem. Phys. Lett. 26, 25 (1974).

[14] J. M. Dyke, L. Golob, N. Jonathan, A. Morris, and M. Okuda, J. Chem. Soc. Faraday Trans. II 70, 1828 (1974).

[15] R. J. Celotta, S. R. Mielczarek, and C. E. Kuyatt, Chem. Phys. Lett. 24, 428 (1974).

[16] N. Swanson and R. J. Celotta, Phys. Rev. Lett. 35, 783 (1975).

[17] J. C. D. Brand, K. J. Cross, and A. R. Hoy, Can. J. Phys. 56, 327 (1978).

[18] R. S. Mulliken, Rev. Mod. Phys. 14, 204 (1942).

[19] A. D. Walsh, J. Chem. Soc. J. Chem. Soc. 1953, 2266.

[20] I. Fischer-Hjalmars, Ark. Fys. 11, 529 (1957).

[21] S. D. Peyerimhoff and R. J. Buenker, J. Chem. Phys. 45, 3682 (1966); 47, 1953 (1967).

[22] E. F. Hayes and G. V. Pfeiffer, J. Am. Chem. Soc. 90, 4773 (1968).

[23] C. Petrongolo, E. Scrocco, and J. Tamasi, J. Chem. Phys. 48, 407 (1968).

[24] S. Rothenburg and H. F. Schaefer, Mol. Phys. 21, 317 (1970).

[25] L. C. Snyder and H. Basch, Molecular Wave Functions and Properties (Wiley, New York, 1972).

[26] P. J. Hay and W. A. Goddard, Chem. Phys. Lett. 14, 46 (1972).

[27] P. J. Hay, T. H. Dunning, Jr., and W. A. Goddard III, Chem. Phys. Lett. 23, 457 (1973); J. Chem. Phys. 62, 3912 (1975).

[28] W. A. Goddard III, T. H. Dunning, Jr., W.J. Hunt, and P. J. Hay, Acc. Chem. Res. 6, 368 (1973).

[29] H. Sambe and R. H. Felton, J. Chem. Phys. 61, 3862 (1974).

[30] H. Basch, J. Am. Chem. Soc. 97, 6047 (1975).

[31] D. P. Chong, F. G. Herring, and D. McWilliams, J. Electron Spectrosc. Relat. Phenom. 7, 445 (1975).

[32] R. P. Messmer and D. R. Salahub, J. Chem. Phys. 65, 779 (1976).

[33] P. W. Langhoff, C. T. Corcoran, J. S. Sims, F. Weinhold, and R. G. Glover, Phys. Rev. A 14, 1042 (1976).

[34] C. T. Corcoran and P. W. Langhoff, J. Math. Phys. 18, 651 (1977).

[35] P. W. Langhoff, "The Stieltjes-Tchebycheff Approach to Molecular Photoionization Studies," in Electron-Molecule and Photon-Molecule Collisions, edited by T. N. Rescigno, B. V. McKoy, and B. Schneider (Plenum, New York, 1979), pp. 183–224.

[36] T. N. Rescigno and P. W. Langhoff, Chem. Phys. Lett. 51, 65 (1977).

[37] T. N. Rescigno, C. F. Bender, B. V. McKoy, and P. W. Langhoff, J. Chem. Phys. 68, 970 (1978).

[38] N. Padial, G. Csanak, B. V. McKoy, and P. W. Langhoff, J. Chem. Phys. 69, 2992 (1978).

[39] A. Orel, T. N. Rescigno, B. V. McKoy, and P. W. Langhoff, J. Chem. Phys. 72, 1265 (1980).

[40] A. Gerwer, C. Asaro, B. V. McKoy, and P. W. Langhoff, J. Chem. Phys. 72, 713 (1980).

[41] P. W. Langhoff, A. Gerwer, C. Asaro, and B. V. McKoy, Int. J. Quantum Chem. Symp. 13, 645 (1979).

[42] T. N. Rescigno, A. Gerwer, B. V. McKoy, and P. W. Langhoff, Chem. Phys. Lett. 66, 116 (1979).

[43] P. W. Langhoff, S. R. Langhoff, and C. T. Corcoran, J. Chem. Phys. 67, 1722 (1977).

[44] P. W. Langhoff, A. E. Orel, T. N. Rescigno, and B. V. McKoy, J. Chem. Phys. 69, 4689 (1978).

[45] Geoffry R. J. Williams and P. W. Langhoff, Chem. Phys. Lett. 60, 201 (1978).

[46] T. H. Dunning and J. P. Hay, in Modern Theoretical Chemistry, edited by H. F. Scahefer III (Plenum, New York, 1976), Vol. 3, Chap. 1.

[47] H. F. Schaefer III, The Electronic Structure of Atoms and Molecules (Addison-Wesley, Reading, Mass., 1972).

[48] H. Lefebvre-Brion, C. Moser, and R. K. Nesbet, J. Mol. Spectrosc. 13, 418 (1964).

[49] H. P. Kelly, Phys. Rev. 136, B896 (1964).

[50] P. W. Langhoff, M. Karplus, and R. P. Hurst, J. Chem. Phys. 44, 505 (1966).

[51] W. J. Hunt and W. A. Goddard III, Chem. Phys. Lett. 3, 414 (1969).

[52] J. Schirmer, W. Domcke, and L. S. Cederbaum, J. Phys. B 11, 1901 (1978).

[53] A. Burgess and M. J. Seaton, Mon. Not. R. Astron. Soc. 120, 121 (1960).

[54] D. R. Bates and A. Damgaard, Astrophys. J. 242, 14 (1949).

[55] C. T. Corcoran and P. W. Langhoff, Chem. Phys. Lett. 41, 609 (1976).

[56] P. W. Langhoff, "Stieltjes-Tchebycheff Moment-Theory Approach to Photoeffect Studies in Hilbert Space," in Theory and Application of Moment Methods in Many-Fermion Systems (Plenum, New York, 1980), pp. 191–212.

[57] R. H. Hughes, J. Chem. Phys. 24, 131 (1956).

[58] We thank W. A. Goddard for helpful private remarks in this connection.

[59] M. S. Banna, D. C. Frost, C. A. McDowell, L. Noodleman, and B. Wallbank, Chem. Phys. Lett. 49, 213 (1977).

[60] K. Siegbahn, C. Nordling, G. Johansson, J. Hedman, P. F. Hedén, K. Harmin, V. Gelius, T. Bergmark, L. O. Werme, R. Manne, and Y. Baer, ESCA Applied to Free Molecules (North-Holland, Amsterdam, 1969).

[61] D. M. Barrus, R. L. Blake, A. J. Burek, K. C. Chambers, and A. L. Pregenzer, Phys. Rev. A 20, 1045 (1979).